



Effect of axial displacement on non-circular tube shaping in hydroforging

Jeremy J. Fischer¹ · Chetan P. Nikhare¹

Received: 26 April 2022 / Accepted: 23 May 2022 / Published online: 25 June 2022
© The Author(s), under exclusive licence to Springer-Verlag France SAS, part of Springer Nature 2022

Abstract

Tube hydroforging with non-circular shaping has been conducted to show the deformation mechanics of an AHSS tube. In this paper, the tube was hydroforged in a multistage FEA simulation to show the effects of axial forging distance on noncircular cross-sections during hydroforging. The tube will be allowed to expand with a ramped internal pressure, then be shaped to a certain expansion ratio by the axial compression in the forging step and finally be shaped into either a square or an equilateral triangle shaped cross-section. It was observed that triangular shaped models have a greater resistance to thickness loss than the square shaped models. The forging die distance for both square and triangular shaping models each influence the maximum amount of shaping die distance for the process. The simulations show that as the forging die distance increases, the lateral radius increases for both the square and triangular shaped models. For the square shaped models, there is an uncorrelated relationship between the vertical and horizontal longitudinal radii but is correlated in the equilateral triangle configurations. The thickness distributions for the triangular shaped configurations show greater stability in the deformed wall portion than the square shaped configurations. All the model setups failed due to wrinkling, except the triangular shaped model with 20 mm of axial displacement, which failed due to bursting.

Keywords Hydroforging · Bulging · Ramped pressure · Numerical simulation · Shaping · Forging

1 Introduction

There is a paramount demand for reduced material parts in all industries that require metal tubes. For example, in the automotive industry sheet metal parts make an immense contribution for the weight of the vehicle. These tubular sheet metal components take up several parts of the vehicle such as the: cam shafts, engine cradles, and anti-roll bars. To create these tubular parts tube forming is one of the primary processing techniques which is further partitioned depending on the shaping requirements of area expansion or area reduction. Tube forming has been used for modifying tube cross sections and has been an enticing manufacturing method to form numerous hollow components. The normal process for tube forming is conducted by reduction and expansion of the parts cross-section and by bending the walls of the component by use of either rigid mandrel tooling or by fluid pressure. Earlier works have showed that acknowledging the

forming history of the tube is relevant to knowing if the hollow component will fail during the forming process [1–3]. Over the past decade tube hydroforging was proposed as an alternative tube forming process that can expand/swell the hollow parts using a minimal amount of fluid pressure. The tubes circular area can expand further by providing axial compression while the tube is pressurized. The advantages of the hydroforging process is that, the friction coefficient of the inner tube is removed, and this process does not have any tooling degradation. Small alterations to the fluid medium pressures can make the tubular component swell to different proportions or form to a different final geometry. The process controls of upper die displacement and the wall crushing displacement of the hydroforging process were observed in this study. A DP280 tube was studied to show the effects of tube formability considering; buckling, wrinkling, folding, and bursting that could occur when wall shaping is applied [4–6]. Previous research on material flow during plastic deformation while considering the geometrical damage prior, displays the effects of additional plastic deformation due to axial compression [7–10]. There is little information on multistage hydroforging processes

✉ Chetan P. Nikhare
cpn10@psu.edu

¹ Penn State Erie–The Behrend College, Erie, PA, USA

to form noncircular tube cross-sections [10–14]. The upper die displacement varies the wall shaping distance and has a noticeable effect on the displacement distance to enable the folding defect. The influence of the upper die displacement for noncircular shaped tubes is favorable depending on the manufacturing application and formability of the material, which is expanded upon in the results. In this paper, the analysis is provided on how the axial die displacement affects the cross-section ductility when subjected to cross section reduction after expansion from the shaping step. The forming process where the buckling potential of metal tubular parts is utilized for cross section alterations in both longitudinal and lateral directions is called multistage hydroforging. In this forming process, the tube is set in a chamber that sets the boundaries of the desired expansion shape. Then the two axial punches compress the tube while the fluid inside of the tube is pressurized internally to swell the tube into the predetermined shape. The walls of the chamber then move inward crushing the tube to the desired shape. To study the effects of deformation in multistage hydroforging, the tube was first pressurized internally to initiate bulging, then pressure was relieved and was axially compressed to expand the tube. Four settings were used for the die displacement, 30, 35, 40, and 45 mm of axial displacement were the only variables modified in the simulation. The wall shaping dies were setup in two configurations, a square shape, and an equilateral triangular shape for wall shaping step. This multistage forming process was used to form the tube, then was further analyzed on how it could be modified by the parameters of the system.

2 Numerical methodology and simulations

2.1 Tube mechanical properties

The material simulated in the numerical analysis is a Dual Phase Steel DP280. The true tensile stress–strain curve for the DP280 is displayed in Fig. 1 which was imported as plasticity data for the numerical simulations with the isotropic hardening assumption. The true tensile stress–strain curves were found using the power law as shown in Eq. 1 [15].

$$\sigma = K \varepsilon^n \quad (1)$$

where, σ is the true stress, K is the materials strength coefficient, ε is the true strain, and n is the materials strain hardening exponent. The mechanical properties of DP280 are given in Table 1 and were acquired from [16].

2.2 Hydroforging setup

The setup for the numerical simulation is shown in Fig. 2(a–c). The geometry of the tube for every simulation ran was

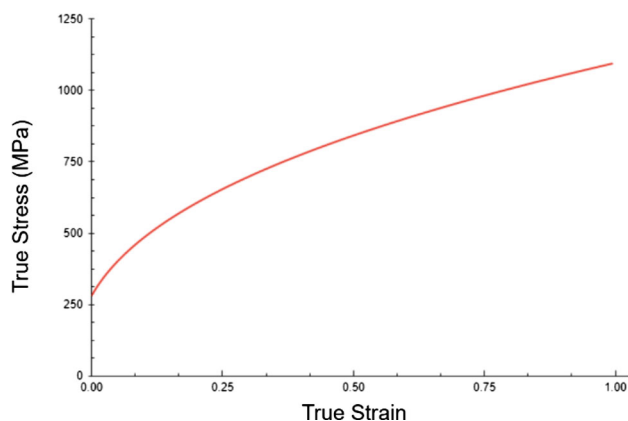


Fig. 1 True stress–strain curve for Dp280

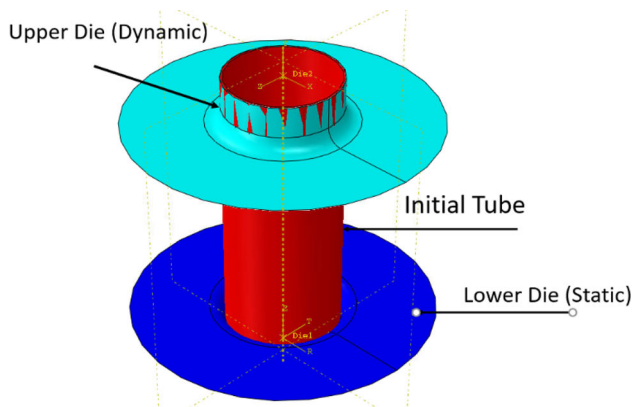
Table 1 Power law parameters for Dp280 [16]

Yield strength (MPa)	280
Strength coefficient “K” (MPa)	1082
Tensile strength (MPa)	600
Young’s modulus (GPa)	210
Density (kg/m ³)	7800
Poisson’s ratio	0.3
Strain hardening exponent	0.4

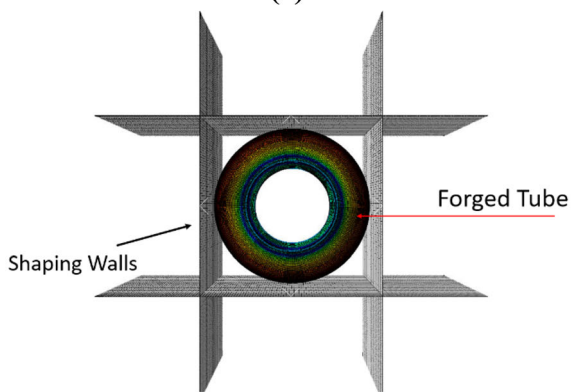
done with models of 38.1 mm in outer diameter, 100 mm in length, and a wall thickness of 0.7112 mm [17, 18]. In this multistage FEA analysis, the upper and lower forging dies hold the tube along with the shaping walls. A pressurized fluid medium then increases its pressure from zero to the required pressure at a constant rate. As the tube is constrained by the upper and lower dies as rigid bodies, the only region for the tube to expand or swell is the die opening of 50 mm between the upper and lower dies. Once the target pressure has been reached, the tube releases a small amount of pressure, then the upper die proceeds to move down the length of the tube by a variable setting to further expand the tubes walls.

After the upper die has finally reached its target stroke and completed the forging step, the shaping process begins. The shaping process is where the gray walls in Fig. 2(b and c) move towards the center of the tube, and the pressure is then instantaneously increased. The walls are used to shape the bulged tube to a noncircular shape by crushing the outer walls of the tube. Once the dies reach the target displacement value, the shaping step ends. The final deformed shape of the initial tube are portrayed in Fig. 3(a–c).

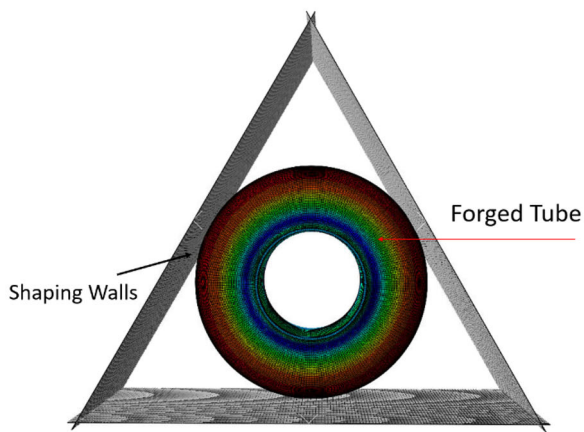
The deformed tubes in Fig. 3(b and c) are considered finished when the tube’s walls are completely flat and do not begin to fold or wrinkle when subjected to greater displacement. When folding occurs the simulations results are



(a)



(b)

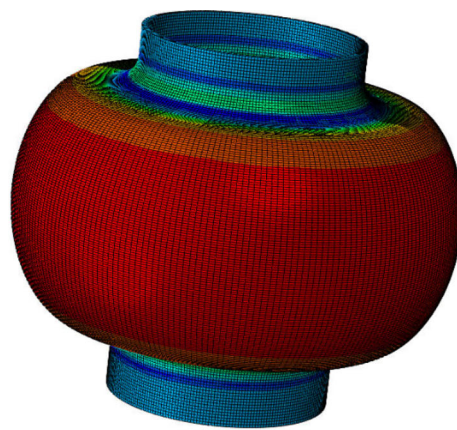


(c)

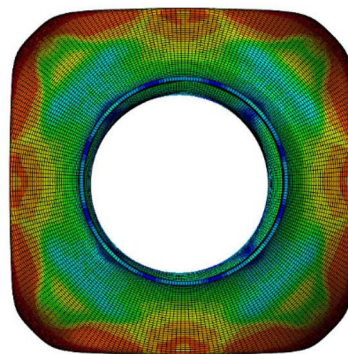
Fig. 2 a Isometric view for hydroforming with axial dies b top view of hydroforming for square shaping, c top view of hydroforming for triangular shaping

recorded to that specific time step and the results are analyzed at the frame before failure.

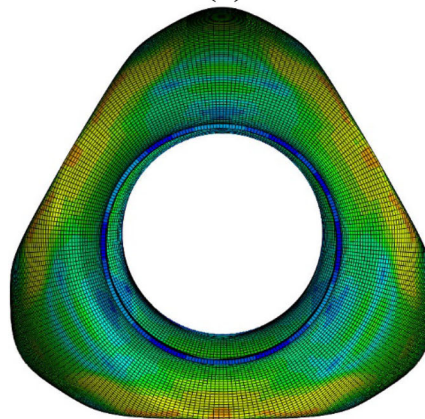
Figure 4a displays pressure in the bulging step increases from zero to the specified bulging pressure “ramp” (red line). The purple line is defined as the constant pressure section, because the pressure remains the same as time increases.



(a)



(b)



(c)

Fig. 3 a Isometric view for final tube shape at end of forging step b top view of tube for square shaping, c top view of tube for triangular shaping

Figure 4b combines both pressures into a multistage hydroforming simulation. Figure 4a shows that the bulging step is a ramped pressure up until the target pressure is reached. The pressure then decreases instantaneously, and the upper die begins its displacement downwards. This is used to allow more expansion to be achieved at the cost of the length of the tube. Once the upper die has reached its target stroke, the shaping step starts, and the pressure is instantaneously

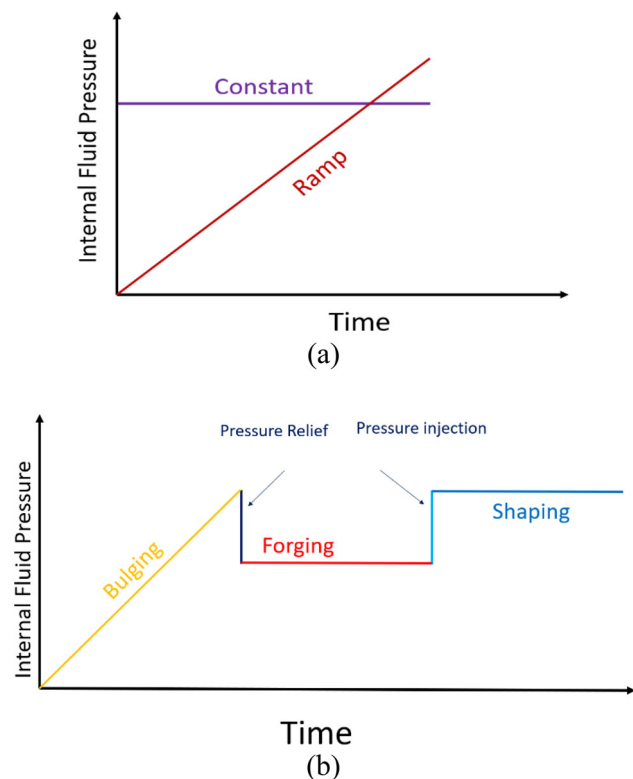


Fig. 4 a Graphical interpretation of the difference in ramped pressure and constant pressure, and b internal pressure with respect to time showing multi stage numerical analysis

Table 2 Fluid pressures for each step

Step	Fluid pressure (MPa)
Bulging	18.75
Forging	17.25
Shaping	18.75

brought back to the peak of the ramped pressure step. The shaping dies then move inward to form the tube walls. The dies move inward from the edge of the expanded tube till the walls have moved inward to a maximum of 12.5 mm of displacement from the walls starting position. The pressure from each step is shown in Table 2. The simulations are stopped whenever any defects occur before the 12.5 mm displacement is reached for the shaping walls. The uniform fluid pressures for each step following pressure relief and pressure injection are shown in Table 2.

Table 2 directly represents the pressure steps shown in Fig. 4b, where pressure is relieved for the forging step, and pressure is injected for the shaping step. The models that were studied in this paper are shown in Table 3, with their configuration details listed in the columns for each case.

Table 3 shows the model configurations, the settings for either equilateral triangle shaping or square shaping, and the

Table 3 Different studied cases with corresponding bulging and shaping pressures

Cases	Number of walls	Wall orientation	Upper die displacement
SQR_S10	4	90°	10 mm
SQR_S20	4	90°	20 mm
SQR_S30	4	90°	30 mm
SQR_S35	4	90°	35 mm
SQR_S40	4	90°	40 mm
SQR_S45	4	90°	45 mm
TRG_S10	3	60°	10 mm
TRG_S20	3	60°	20 mm
TRG_S30	3	60°	30 mm
TRG_S35	3	60°	35 mm
TRG_S40	3	60°	40 mm
TRG_S45	3	60°	45 mm

upper die displacement. The model cases are directly related to the tube shape and the upper die displacement. The shape is either defined by TRG for triangular shaping or SQR for square shaping. The die displacement for the case is noted by “S#” which the # represents the upper die displacement in millimeters. Note that the pressure settings for all cases remain the same during all steps in the numerical analysis.

ABAQUS/CAE finite element analysis software code (version 6.13-2) was used to simulate all considered hydroforming models. 3D Models were used to make an accurate experimental representation of the multistage hydroforming process. Both upper and lower dies, as well as the crushing walls are assigned as rigid shell bodies. The tube was assigned as a solid deformable body modeling the material properties of DP280 used in Table 1. The tube has meshed with C3D8R brick elements with a global element size of 0.5 mm. The elements chosen to provide greater three-dimensional accuracy, while being computationally effective for the explicit/dynamic analysis. A convergence study is not needed, because additional refinement will not significantly impact the results within 10%. Frictionless contact was utilized between the inner surface of the dies, the shaping walls, and the outer tube face using kinematic surface to surface contact. No experimental analysis has been conducted to compare with the simulation results for this paper.

3 Results

3.1 Square shaping models

The square shaping models have four walls that travel into the expanded tube after the forging step. Figure 5 shows how

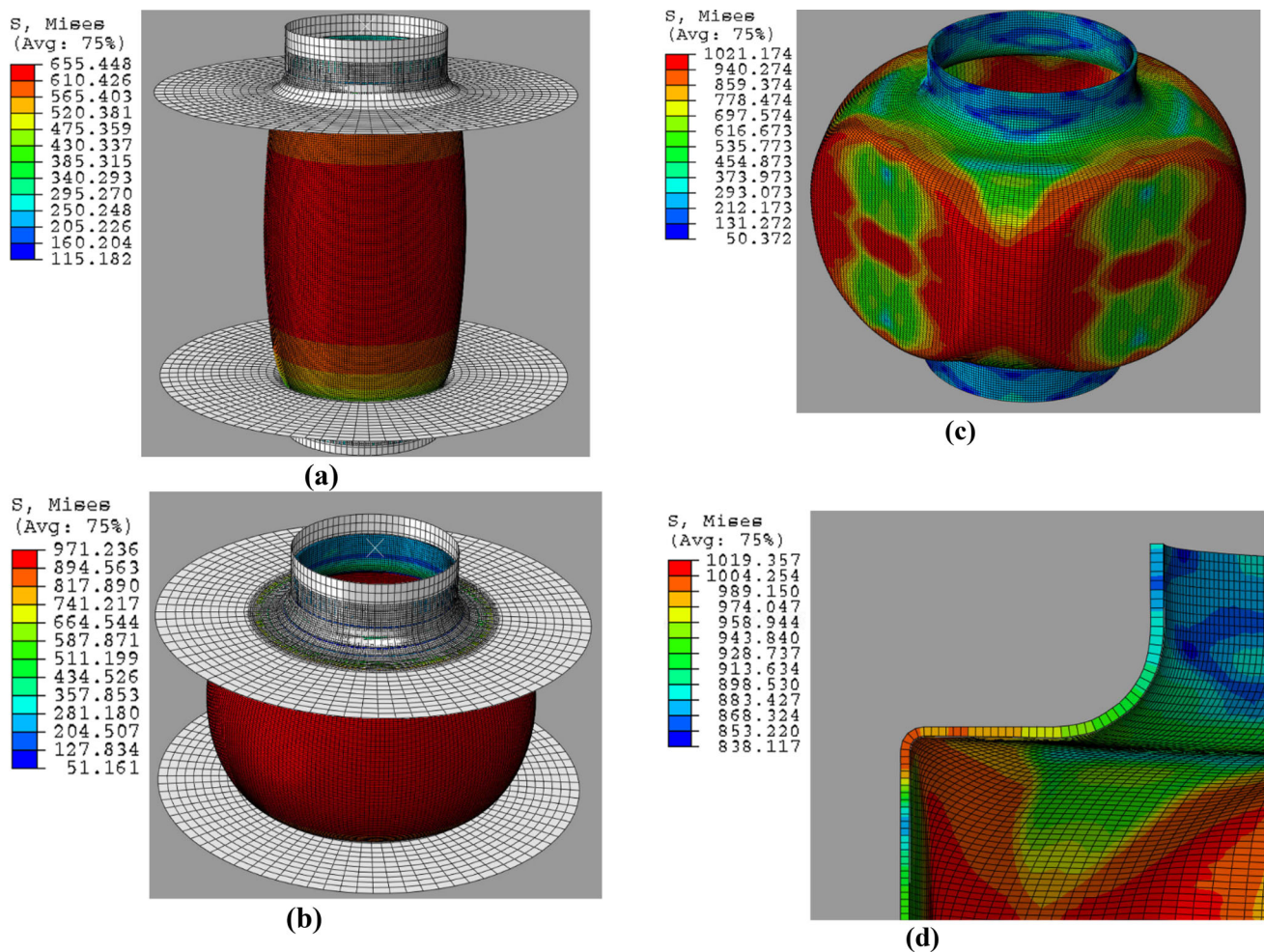


Fig. 5 Outer wall deformation mechanics of square shaping model SQR_S30 for **a**, end of bulging step, **b** End of shaping step, **c** Finished shaping step at 5.75 mm, and **d** Corner cross section at 5.75 mm

the deformed circular tube from the start eventually form corners from the wall shaping process. It was observed that as the shaping dies increase the displacement, the von mises stress for the tube increases, until wrinkling occurs near the corners of the shaped part.

Figure 6 shows how the wrinkling defect occurs in the square shaping step. As the walls move inwards to shape the tube, too much displacement can lead to the walls wrinkling. The final shaping distances for the square shaping models are shown in Table 4.

The data presented shows that there is a relationship between how the forging displacement affects the shaping displacement for square tube shaping. The results show that the maximum displacement amount of shaping distance can be achieved from 20 mm of upper die displacement in the forging step. From model SQR_S45, it is observed that the lowest amount of shaping die displacement can be achieved, and wrinkle earlier than all the square shaping configurations. A graphical trend for the shaping displacement to the

forging displacement can be observed in Fig. 7. It shows that as the upper die displacement is increased after the 20 mm mark, the amount shaping distance the walls of the tube can withstand decreases.

The models have been observed to find other relationships that can lead to the maximum shaping die displacement, such as the longitudinal and lateral radial measurements. When the shaping step initiates and the dies contact the tube, the corners of the shape begin to take form over displacement, whether it is viewed from the top of the tube, or from the front of the tube. The longitudinal and lateral radii are measured as displayed in Fig. 8.

The longitudinal radius can be described as the measurement of the wall to the upper flat region of the hydroforged tube. The lateral radius is defined as the radius measurement of the corner between the two plates from the top view. The same method is also used in the triangle models. The methods for measuring longitudinal and lateral radius are the same for the triangular shaping configurations. The longitudinal radius

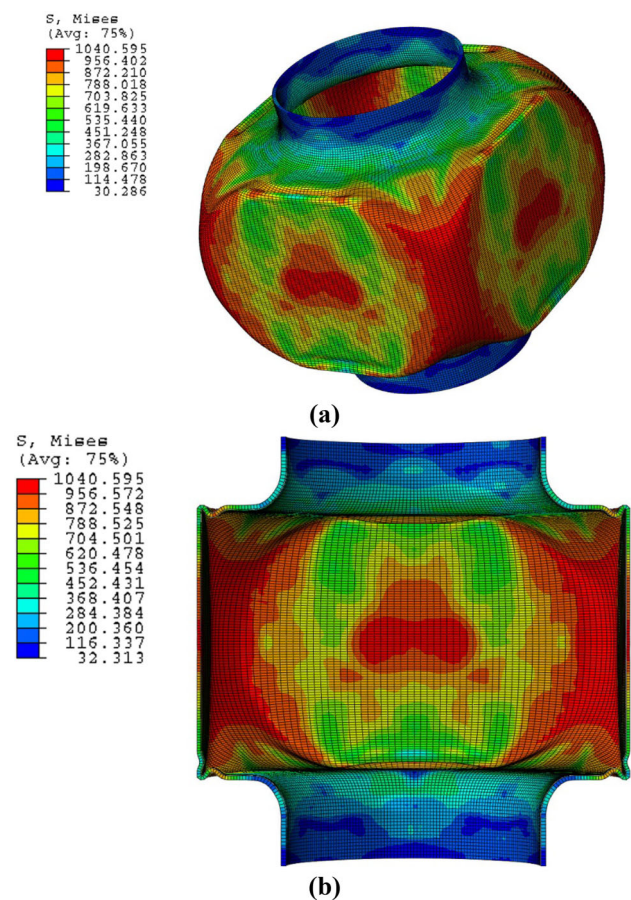


Fig. 6 **a** Isotropic view of sq_r_s30 model wrinkling after excessive shaping displacement, **b** cross-section view

Table 4 Square shaping hydroforging maximum shaping distances

Case	Successful shaping displacement
SQR_S10	5.5 mm
SQR_S20	6.5 mm
SQR_S30	5.75 mm
SQR_S35	5.375 mm
SQR_S40	4.75 mm
SQR_S45	4.00 mm

for the square shaping configurations is recorded in Table 5 and is graphically represented in Fig. 9.

The scatterplot shown in Fig. 9 shows that there is an uncorrelated relationship between the horizontal and vertical longitudinal radius. The lateral radius is defined as the radius measurement of the corner between the two plates from the top view. The same method is also used in the triangle models. As with the lateral radius, the end points of the lateral radius have been recorded and graphically represented in Fig. 10 and Table 6.

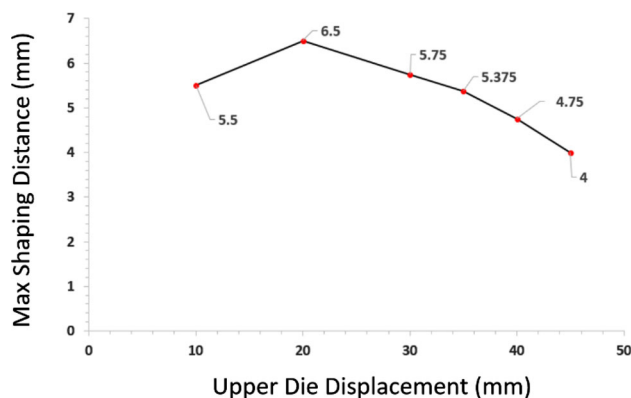


Fig. 7 Marker plot representation of upper die displacement vs max shaping distance for square tube hydroforging

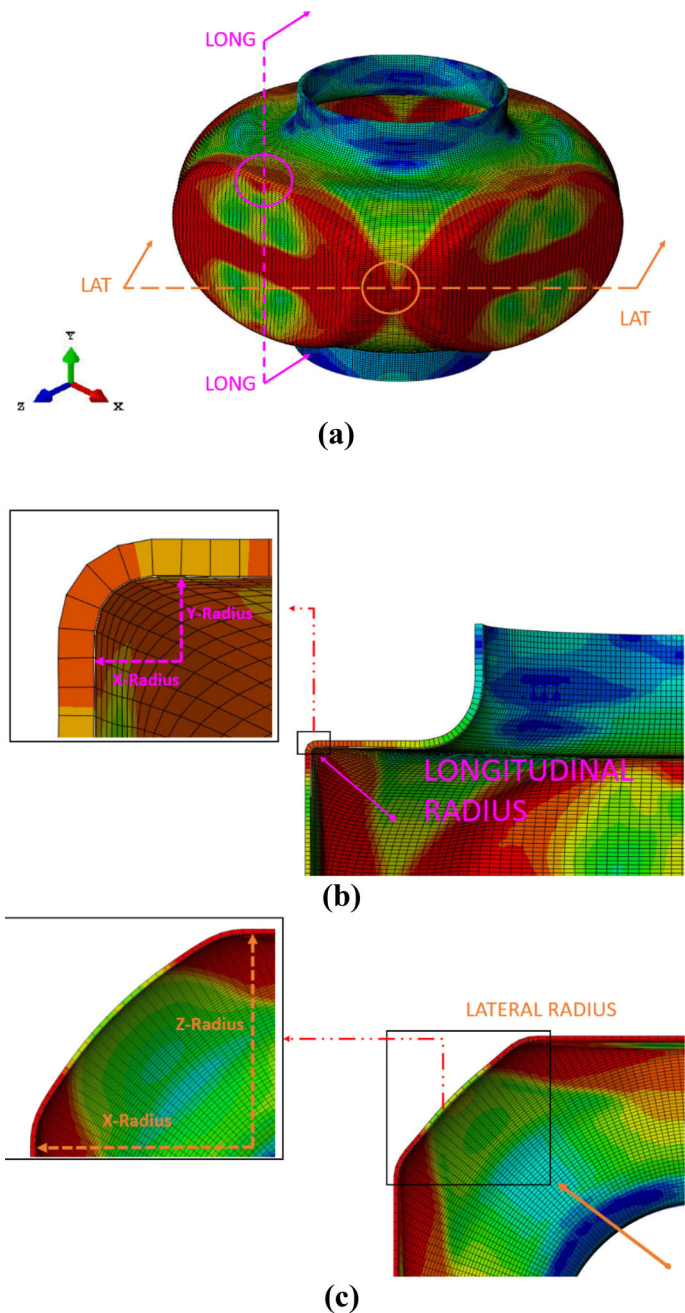
Unlike Fig. 9, for longitudinal radius the lateral relationship shows a positively correlated relationship between the horizontal and vertical lateral radii. Figure 10 also shows that the relationship between the forging die distance and both the vertical and horizontal lateral radius. It can be confirmed that as the upper forging die displacement is increased, the lateral radius (horizontal and vertical) will be larger in magnitude when maximum shaping distance is achieved. Based on Nikhare et al. [17, 18], the thickness distribution from the center of the tube's walls to the opening of the tube has been studied and shown in Fig. 11.

The thickness was observed at the frames before failure in Table 4. It is obvious that as the forging die distance increases, the thickness at the center of the wall will decrease due to thinning from bulging of the tube. Another notable observation is that the thickness for all separate cases appear to follow the same path around 25 mm, which is the location of the flat upper portion of the tube. It can also be observed that the starting thickness for SQR_S10 is far greater than the other models at the start. This means that there is nonlinear relationship somewhere between 10–20 mm of forging die displacement, where the thickness rapidly decreases, and then eventually becomes steady as forging die displacement increases.

3.2 Triangular shaping models

The deformation mechanics of the triangular shaping setup shows an obvious change in cornering due to the shaping dies being oriented at a sharper angle. The angle orientation also gives a notably larger lateral radius which can be observed in Fig. 12. Compared to Fig. 5, for the same amount of wall displacement, there is less von mises stress per millimeter of displacement from the shaping dies with the triangular models. It was also observed that the greater von mises stress is located in the walls of the model instead of in the corners. Also, all the triangular shaping models wrinkling initiates in

Fig. 8 **a** Location of the longitudinal radius for square hydroforming models, **b** Longitudinal radius measurement distance, **c** Lateral radius measurement distance



the lower forging die, instead of the upper forging die. As with the square shaping models, the final shaping diameters have been recorded in Table 7 for the triangular models.

The results in Table 7, show a similar trend to the results from Table 4. For the triangular case, the maximum shaping distance can be obtained at a forging die distance of 30 mm. Like the trend in Table 4, the smallest shaping distance can be achieved when the forging die displacement is at 45 mm, as shown in the TRG_S45 model. All the triangular shaping models failed from wrinkling, except for TRG_S20 which failed from bursting, and is further expanded upon in the

simulation results. The relationship between the shaping distance and the upper die displacement has been plotted in Fig. 13.

Compared to Fig. 7, the results from the marker plot portray a bell-curve trend for upper die displacement and maximum shaping distance. The graph shows that from 20–30 mm there is a large jump in the allowable shaping distance compared to any other two points. The line trend after the 30 mm upper die displacement mark, shows that the maximum shaping distance decreases at a steady rate compared to the upper forging die displacement. For the upper forging die

Table 5 Longitudinal radius measurements for horizontal and vertical radii In Square Models

Case	Longitudinal radius (X)	Longitudinal radius (Y)
SQR_S10	1.012 mm	1.131 mm
SQR_S20	1.41081 mm	1.377 mm
SQR_S30	1.2503 mm	1.569 mm
SQR_S35	1.529 mm	1.24 mm
SQR_S40	1.959 mm	1.203 mm
SQR_S45	1.233 mm	1.459 mm

Table 6 Lateral radius measurements for horizontal and vertical radii in square models

Case	Lateral radius (X)	Lateral radius (Z)
SQR_S10	5.316 mm	5.682 mm
SQR_S20	8.681 mm	8.234 mm
SQR_S30	10.979 mm	10.473 mm
SQR_S35	13.32 mm	12.821 mm
SQR_S40	16.954 mm	16.452 mm
SQR_S45	23.471 mm	33.557 mm

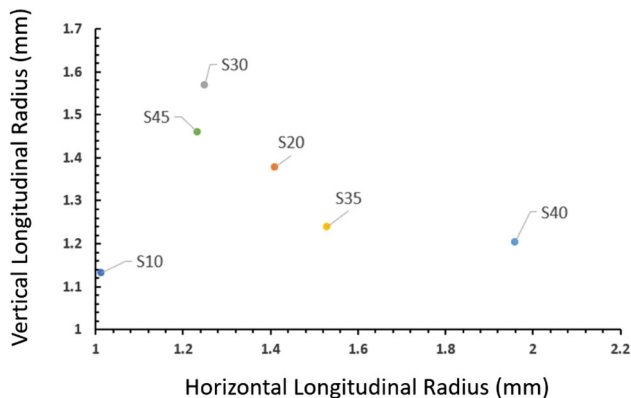


Fig. 9 Horizontal Vs vertical longitudinal radius for square tube hydroforming simulations

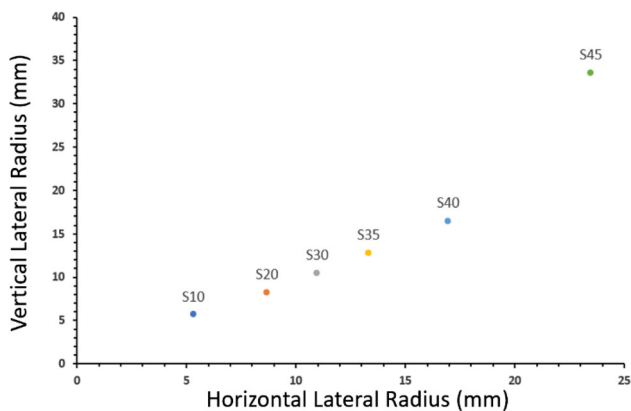


Fig. 10 Horizontal Vs vertical lateral radius for square tube hydroforming simulations

displacement, the maximum shaping distance decreases by 0.75 mm for every 5 mm of distance the upper die displaces, after the maximum shaping distance has been reached.

The longitudinal and lateral radii have also been measured to show a greater significance in rounding radius compared to the square hydroforming models. For the triangular shaping models, the same methods were utilized with the square shaping models for measuring longitudinal and lateral radii.

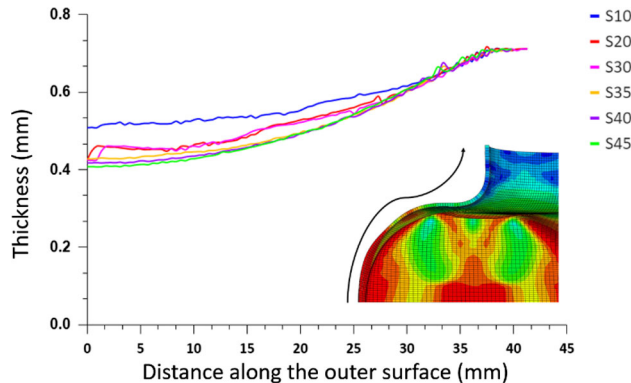


Fig. 11 Thickness distribution for square shaping hydroforming simulations

The locations of the longitudinal and lateral radius measurements are shown in Fig. 14 for triangular shaping models.

The longitudinal radius measurements for the triangular shaped hydroforming models are displayed in Table 8 and Fig. 15.

The longitudinal radius measurements for the triangular hydroforming simulations show an uncorrelated trend between horizontal and vertical longitudinal radius. However, notable observations can be made between the relationship of forging die displacement and the absolute difference between horizontal and vertical longitudinal radii. The TRG_S20 model has a notably large longitudinal radius, which is due to failure from bursting instead of wrinkling. This confirms that there is a considerable variation between horizontal and longitudinal radius after the 20 mm of upper die displacement has been reached. The longitudinal radius for both horizontal and vertical radii both have a trend to decrease in radius as the forging die distance increases, with the TRG_S40 model being an outlier in this case for just the horizontal radius. The triangular shaping simulations do not need mesh refinement to obtain more data because a trend has been established between the forging die distance and the longitudinal radius. The lateral radius for the triangular shaped hydro-forming models are shown in Table 9 and Fig. 16.

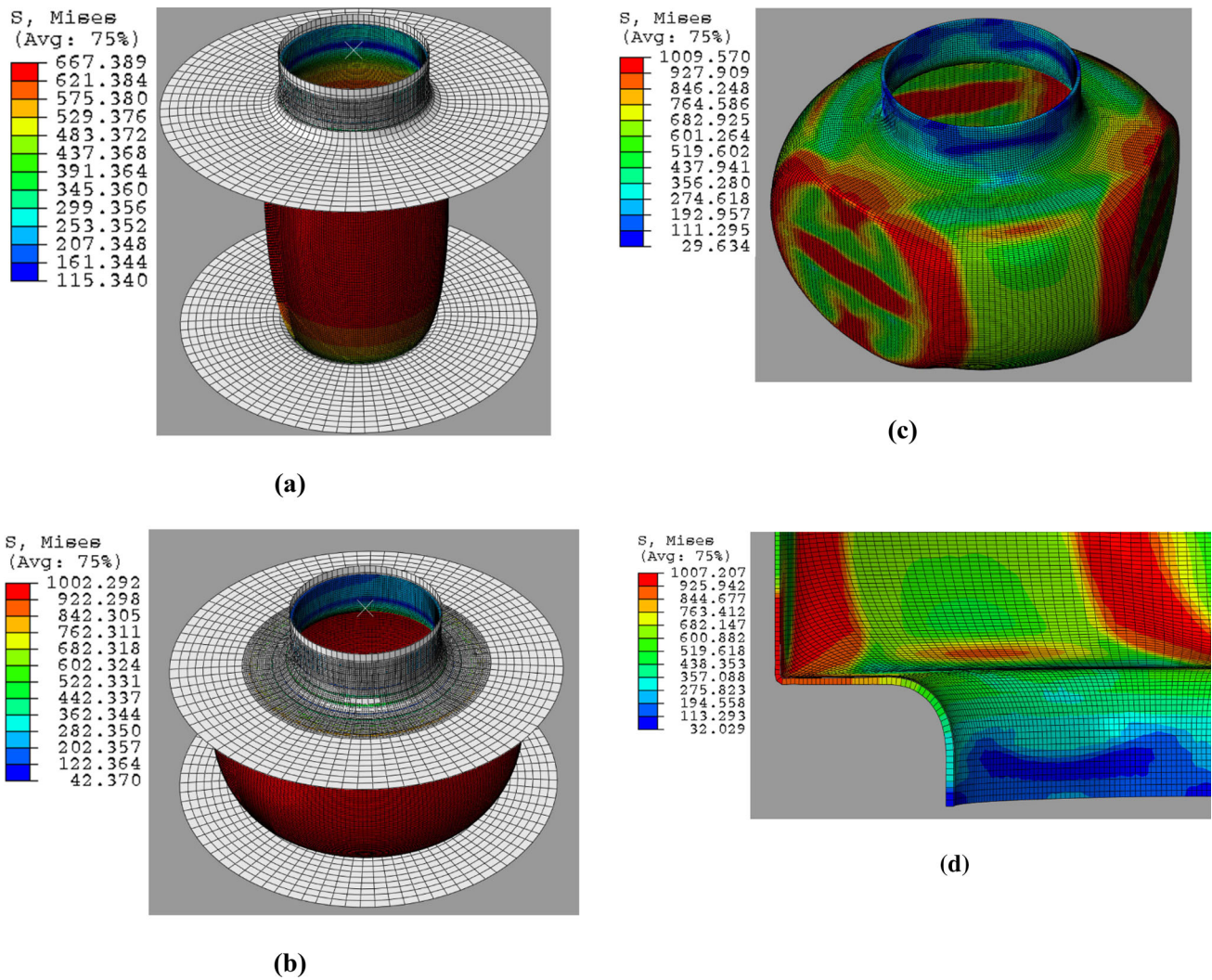


Fig. 12 Outer wall deformation mechanics of triangular shaping model *trg_s35* for **a**, end of bulging step, **b** end of shaping step, **c** finished shaping step at 5.75 mm, and **d** corner cross section at 5.75 mm

Table 7 Triangular Shaping Hydroforming Maximum Shaping Distances

Case	Total shaping displacement
TRG_S10	5.0 mm
TRG_S20	5.375 mm
TRG_S30	6.5 mm
TRG_S35	5.75 mm
TRG_S40	5.0 mm
TRG_S45	4.25 mm

The trend the lateral radius in Fig. 16 follows the same pattern as the square shaping in Fig. 10. As the forging die displaces the lateral radius for both horizontal and vertical radii will increase as a result. The lateral radius in the triangular shaping configurations is also notably greater than the square shaping lateral radii in Fig. 10.

The thickness distribution for the triangular hydroforming models is graphically represented in Fig. 17. For the triangular shaping thickness distribution, it can be confirmed that as the distance of the forging die increases, the thickness of the tube’s walls will decrease. There is also a notable decrease in thickness from the starting point of the middle of the tube, which happens between 10 and 20 mm of upper die displacement. Also, compared to Fig. 11, the wall thickness distribution is smoother near the starting point of the outer surface.

3.3 Comparison between configurations

The square shaping simulations compared with the triangular shaping simulations have shown that square shaping is more sensitive to the forging die distance than triangular shaping. This is obviously compared to the Tables 4 and 7 and is

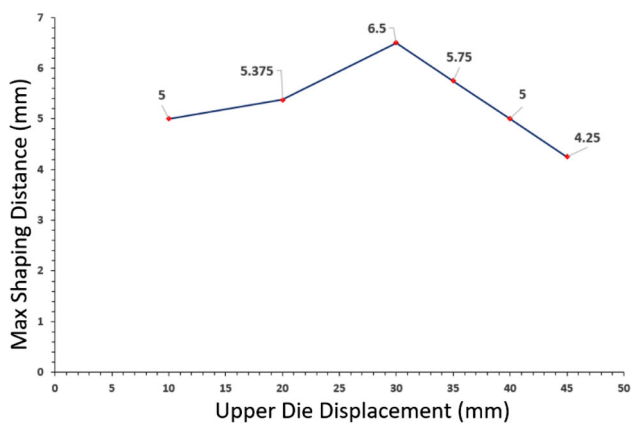
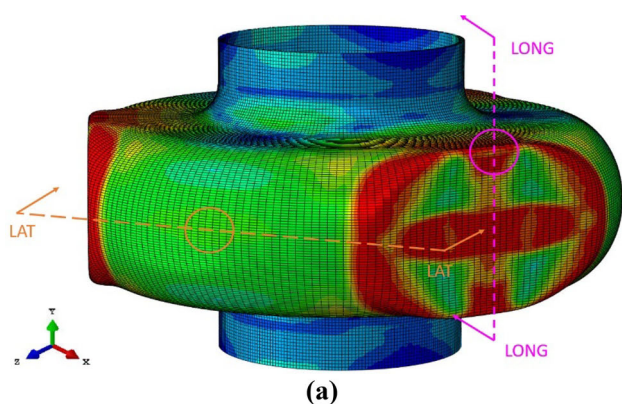
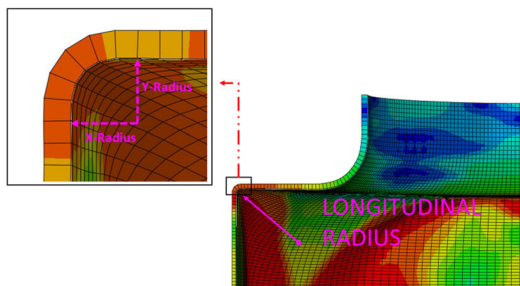


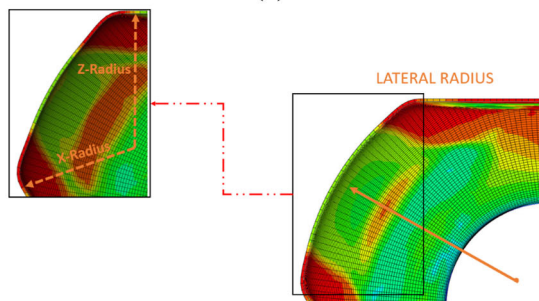
Fig. 13 Marker plot representation of upper die displacement vs max shaping distance for triangular tube hydroforging



(a)



(b)



(c)

Fig. 14 a Location of the longitudinal radius for triangular hydroforging models, b longitudinal radius measurement distance, c lateral radius measurement distance

Table 8 Longitudinal radius measurements for horizontal and vertical radii in triangular models

Case	Longitudinal radius (X)	Longitudinal radius (Y)
TRG_S10	1.660 mm	1.458 mm
TRG_S20	3.456 mm	2.980 mm
TRG_S30	0.976 mm	0.886 mm
TRG_S35	0.627 mm	0.784 mm
TRG_S40	0.630 mm	0.743 mm
TRG_S45	0.605 mm	0.724 mm

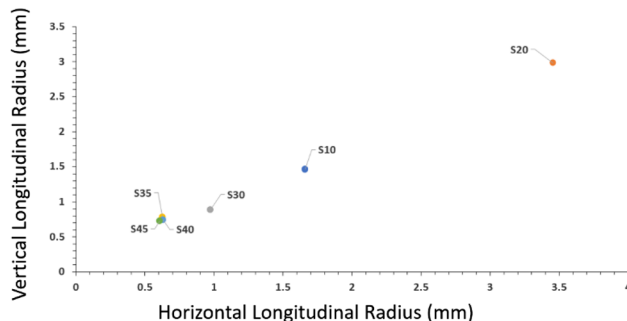


Fig. 15 Horizontal Vs vertical longitudinal radius for triangular tube hydroforging simulations

Table 9 Lateral radius measurements for horizontal and vertical radii in triangular models

Case	Lateral radius (X)	Lateral radius (Z)
TRG_S10	12.923 mm	23.278 mm
TRG_S20	15.844 mm	26.862 mm
TRG_S30	16.276 mm	29.386 mm
TRG_S35	19.479 mm	33.112 mm
TRG_S40	21.982 mm	37.472 mm
TRG_S45	24.783 mm	42.325 mm

hypothesized to be due to the number of walls and the shaping dies orientation for the hydroforging process. The lateral radius measurements between the two models have shown that the triangular shaped models decrease with respect to the upper die displacement in the forging step. The lateral displacement in the square shaping models shows an uncorrelated trend with respect to the upper die displacement, which can be taken advantage of in the industry to provide similar lateral radii with little effects from the forging die distance. The lateral radius in both the square and triangular models both increases with respect to the upper die displacement. This is confirmed by the positive correlation as shown in Figs. 10 and 16. Comparing the values from Tables 6 and 9, it can be observed that the lateral radius in both horizontal and vertical directions is greater in the triangular shaping models

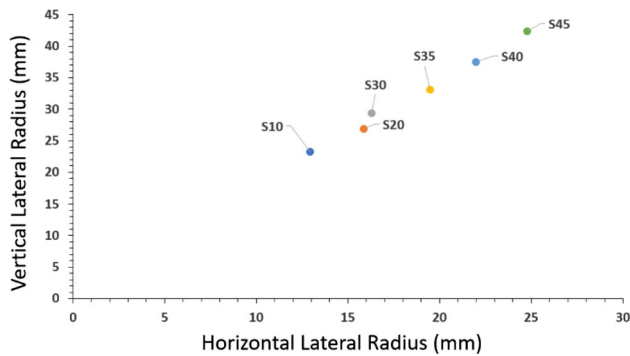


Fig. 16 Horizontal Vs vertical lateral radius for triangular tube hydroforming simulations

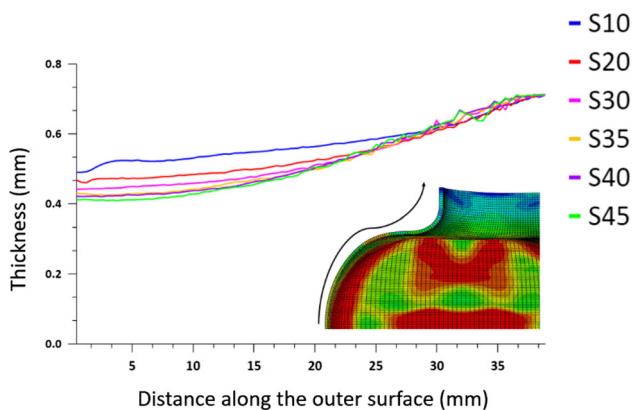


Fig. 17 Thickness distribution for triangular shaping hydroforming simulations

compared to the square shaping models. This is primarily due to the angle at which the dies and the wall meet at, which is attributed to the shape, given that a larger angle between the two walls will lead to a smaller lateral radius. Looking at the thickness distribution data, the square shaping models have a greater loss of initial thickness compared to the triangular shaping models. This difference is only noticeable by ~ 0.1 mm in the values when the two graphs are compared for each upper die setting in the forging step. However, the trend between the two thickness distributions do not seem to change in slope from the distance from the middle of the wall to the upper undeformed portion of the tube. This is most likely because of how the tube walls expand in the bulging and forging steps but are compressed in the shaping step. It can also be said, that only bursting failure occurs in the triangular shaping models for all simulations and should not be forged around 20 mm to prevent bursting failure for triangular tubes.

4 Conclusion

The multistage hydroforming simulation in this study shows how the square and triangular shaped tube wall affects the geometric parameters with respect to the axial die forging distance. The square shaping models was able to achieve a maximum shaping die distance of 6.5 mm at the forging distance of 20 mm. The triangular shaping models had a maximum shaping distance of 6.5 mm at a forging distance of 30 mm. It was confirmed that as the upper die distance is increased in the forging step, the lateral radius for both horizontal and vertical measurements would increase for both setups. Moreover, it was noted that the longitudinal radius only shows a trend in the triangular configurations with respect to the forging die distance, where the square configurations do not show any trend. There is a range of forging die distance for where the maximum amount of shaping distance can be achieved and is at 20 mm for square shaping, and 30 mm for triangular shaping with studied conditions. The square shaping models show greater thickness loss at the same forging die settings than the triangular model settings. Bursting failure only occurs for the TRG_S20 model, where every other model in the simulation failed from the wrinkling defect.

Acknowledgements Authors would like to thank Penn State Erie, The Behrend College for support provided to perform this research and its unique open lab research facility.

Funding Not Applicable.

Availability of data and material Not Applicable.

Code availability Not Applicable.

Declarations

Conflicts of Interests The authors declare no competing interests.

Ethics approval Not Applicable.

Consent to participate Not Applicable.

Consent for publication Not Applicable.

References

- Xu, Y., Ma, Y., Zhang, S., et al.: Numerical and experimental study on large deformation of thin-walled tube through hydroforming process. *Int J Adv Manuf Technol* **87**, 1885–1890 (2016)
- Xia, L.L., Xu, Y., Abd El-Aty, A., Zhang, S.H., Nielsen, K.B., Li, J.M.: Deformation characteristics in hydro-mechanical forming process of thin-walled hollow component with large deformation: experimentation and finite element modeling. *Int. J. Adv. Manufact. Technol.* **104**(9), 4705–4714 (2019)
- Huang, Y.M.: Finite element analysis of tube flaring process with a conical tool. *Int. J. Adv. Manufact. Technol.* **24**, 91–97 (2004)

4. Huang, Y.M.: Elasto-plastic finite-element analysis of the axisymmetric tube-flaring process with conical punch. *Int J. Adv. Manuf. Technol.* **18**(6), 390–398 (2001)
5. Alzahrani, B., Ngaile, G.: Analytical and numerical modeling of thick tube hydroforming. *Procedia Engineering* **81**, 2223–2229 (2014)
6. Müller, K., Stonis, M., Lücke, M., Behrens, B. A.: Hydroforming of Thick-Walled Hollow Aluminum Profiles. In: *Key Engineering Materials*. 504, pp. 181–186. Trans Tech Publications Ltd (2012)
7. Sun, Z., Yang, H.: Development of a finite element simulation system for the tube axial compressive precision forming process. *Int. J. Mach. Tools Manuf* **42**, 15–20 (2002)
8. Yang, H., Zhichao, S., Yingjun, J.: FEM analysis of mechanism of free deformation under dieless constraint in axial compressive forming process of tube. *J. Mater. Process. Technol.* **115**, 367–372 (2001)
9. Nikhare, C.P.: A numerical analysis on microtube hydroforming. *Adv. Mater. Process. Technol.* 1–22 (2021)
10. Sun, L., Lin, C., Wang, G., Chu, G.: Multistage axial hydro-forming sequence of double-stepped tube with large expansion ratio. *Int. J. Lightweight Mater. Manufact.* **3**(2), 172–176 (2020)
11. Chu, G.N., Chen, G., Wang, G.D., Fan, Z.G., Li, H.: Analysis of warping failure in tube hydro-forming. *Int. J. Mech. Sci.* **165**, 105216 (2020)
12. Chu, G.N., Chen, G., Lin, Y.L., Yuan, S.J.: Tube hydro-forming—a method to manufacture hollow component with varied cross-section perimeters. *J. Mater. Process. Technol.* **265**, 150–157 (2019)
13. Chen, G., Yao, S.J., Chen, B.G., Chu, G.N.: Research on tube hydro-forming process of trapezoid-sectional parts. *Int. J. Adv. Manuf. Technol.* **107**(3), 1901–1908 (2020)
14. Chu, G.N., Chen, G., Lin, C.Y., Fan, Z.G., Li, H.: Analytical model for tube hydro-forming: prediction of die closing force, wall thickness and contact stress. *J. Mater. Process. Technol.* **275**, 116310 (2020)
15. Alzahrani, B., Ngaile, G.: Preliminary investigation of the process capabilities of hydroforming. *Materials* **9**(1), 40 (2016)
16. Mahmoud Y. D.: Forming of Advanced High-Strength Steels, *Metalworking: Sheet Forming*, Vol 14B, ASM Handbook, Edited by S.L. Semiatin, ASM International, pp 530–538 (2006)
17. Nikhare, C.P.: Tube Buckling: an Advantage to Tube Shaping. In: *ASME International Mechanical Engineering Congress and Exposition Vol. 52019*, American Society of Mechanical Engineers. pp. V002T02A031 (2018)
18. Nikhare, C.: "Buckling of Tube for Tube Hydroforming. In: *Proceedings of ASME: International Mechanical Engineering Congress and Exposition*. pp. 1–8 (2019)

Publisher's Note Springer Nature remains neutral with regard to jurisdictional claims in published maps and institutional affiliations.